

Communication

# Ultralow Loading Ruthenium on Alumina Monoliths for Facile, Highly Recyclable Reduction of *p*-Nitrophenol

Lorianne R. Shultz<sup>1,2</sup>, Corbin Feit<sup>2,3</sup>, Jordan Stanberry<sup>1</sup>, Zhengning Gao<sup>2,3</sup>, Shaohua Xie<sup>2,4</sup>, Vasileios A. Anagnostopoulos<sup>1</sup>, Fudong Liu<sup>2,4,5</sup> , Parag Banerjee<sup>2,3,5,\*</sup>  and Titel Jurca<sup>1,2,5,\*</sup>

<sup>1</sup> Department of Chemistry, University of Central Florida, 4111 Libra Drive, Orlando, FL 32816, USA; lorishultz@knight.ucf.edu (L.R.S.); Stanberry.jordan@knights.ucf.edu (J.S.); Vasileios.Anagnos@ucf.edu (V.A.A.)

<sup>2</sup> Renewable Energy and Chemical Transformations Cluster, University of Central Florida, 4353 Scorpius Street, Orlando, FL 32816, USA; corbinf@knights.ucf.edu (C.F.); zhengning.gao@airliquide.com (Z.G.); Shaohua.Xie@ucf.edu (S.X.); fudong.liu@ucf.edu (F.L.)

<sup>3</sup> Department of Materials Science and Engineering, University of Central Florida, Orlando, FL 32816, USA

<sup>4</sup> Department of Civil, Environmental, and Construction Engineering, University of Central Florida, Orlando, FL 32816, USA

<sup>5</sup> NanoScience Technology Center, University of Central Florida, Orlando, FL 32826, USA

\* Correspondence: Parag.Banerjee@ucf.edu (P.B.); Titel.Jurca@ucf.edu (T.J.)

**Abstract:** The pervasive use of toxic nitroaromatics in industrial processes and their prevalence in industrial effluent has motivated the development of remediation strategies, among which is their catalytic reduction to the less toxic and synthetically useful aniline derivatives. While this area of research has a rich history with innumerable examples of active catalysts, the majority of systems rely on expensive precious metals and are submicron- or even a few-nanometer-sized colloidal particles. Such systems provide invaluable academic insight but are unsuitable for practical application. Herein, we report the fabrication of catalysts based on ultralow loading of the semiprecious metal ruthenium on 2–4 mm diameter spherical alumina monoliths. Ruthenium loading is achieved by atomic layer deposition (ALD) and catalytic activity is benchmarked using the ubiquitous para-nitrophenol, NaBH<sub>4</sub> aqueous reduction protocol. Recyclability testing points to a very robust catalyst system with intrinsic ease of handling.

**Keywords:** nitrophenol reduction; alumina support; ruthenium catalysis; aqueous pollutant degradation



**Citation:** Shultz, L.R.; Feit, C.; Stanberry, J.; Gao, Z.; Xie, S.; Anagnostopoulos, V.A.; Liu, F.; Banerjee, P.; Jurca, T. Ultralow Loading Ruthenium on Alumina Monoliths for Facile, Highly Recyclable Reduction of *p*-Nitrophenol. *Catalysts* **2021**, *11*, 165. <https://doi.org/10.3390/catal11020165>

Academic Editor: Feng Gao

Received: 1 December 2020

Accepted: 21 January 2021

Published: 25 January 2021

**Publisher's Note:** MDPI stays neutral with regard to jurisdictional claims in published maps and institutional affiliations.



**Copyright:** © 2021 by the authors. Licensee MDPI, Basel, Switzerland. This article is an open access article distributed under the terms and conditions of the Creative Commons Attribution (CC BY) license (<https://creativecommons.org/licenses/by/4.0/>).

## 1. Introduction

Nitroaromatics represent a family of broadly used compounds in industrial processes; for example, in pesticide, fungicide, textile and pharmaceutical manufacturing. Consequently, they are a common pollutant in aqueous industrial effluent, notably displaying acute toxicity and potential carcinogenicity. This has motivated the study of remediation strategies, namely the mild-conditions -NO<sub>2</sub> group reduction to yield their less toxic and synthetically useful aniline (-NH<sub>2</sub>) derivatives. Among this general reaction family, the catalytic reduction of *para*- or 4-nitrophenol (4NP) specifically has emerged as the benchmark test for catalysts—not only for relevant environmental remediation, but also as a universal rapid screening test for heterogeneous catalyst reduction activity [1–3]. Most typically, catalytic reduction of 4NP is conducted in deionized water (DIW) with a large excess of a hydrogen source, such as sodium borohydride (NaBH<sub>4</sub>), which provides surface -H species; H<sub>2</sub> generated by competing NaBH<sub>4</sub> hydrolysis may also play a role under certain conditions. The reaction is readily monitored through Ultraviolet–Visible (UV–Vis) spectrophotometry by tracking the decrease in absorbance at λ<sub>max</sub> = 400 nm, associated with 4-nitrophenolate (4NP<sup>\*</sup>), the anionic derivative of 4NP which forms in the presence of NaBH<sub>4</sub>. Reaction kinetics (*k*<sub>app</sub> = apparent rate) are derived from the slope of ln(*A*/*A*<sub>0</sub>)

which correlate to 4NP\* concentrations ( $C/C_0$ ) (Equation (1)). The reaction is typically described in terms of the Langmuir–Hinshelwood model, and the large excess of  $\text{NaBH}_4$  not only provides an ample H-source, but also creates a pseudo-first-order process, allowing facile interpretation of kinetics [4–6].

$$-k_{app}t = \ln\left(\frac{A}{A_0}\right) = \ln\left(\frac{C}{C_0}\right) \quad (1)$$

Historically, catalytic reduction of 4NP has been promoted primarily with catalytic noble metal nanoparticles [7–12], to a lesser extent with non-noble metal nanoparticles [13–17], and more recently nonmetal species [18–21]. A significant majority of these catalyst systems are submicron- or even a few-nanometer-sized colloidal particles. Although very catalytically efficient for lab-scale testing and generation of fundamental knowledge, the use of nanocatalysts in the environment can be challenging to manage, and their fate and transport are complex and may pose hazards [22–28]. We endeavored to develop a robust and more applicable nitroaromatic reduction catalyst, which circumvents the need for submicron or even ultrasmall colloidal nanoparticles. Herein, we report the fabrication of catalysts based on ultralow loading of semiprecious metal ruthenium on 2–4 mm diameter spherical alumina monoliths. Controllable, ultralow ruthenium loading is achieved by atomic layer deposition (ALD). ALD is a self-limiting technique which provides a highly precise and reproducible coating thickness. Because of the high level of control afforded, it is not surprising that ALD is emerging as a powerful tool for catalyst synthesis. ALD-synthesized catalysts have been previously studied for hydrolysis reactions [29–31]; notably, Jiang et al. reported the use of an ALD-Ni coated catalyst for nitrophenol reduction [32]. Ruthenium was chosen due to its well-established catalytic activity in reduction reactions [33–38], lower cost compared to Pd and Au catalysts which dominate nitroaromatic reductions, and the availability of a well-defined ALD process for Ru films, as developed by one of our groups [39]. The ALD-Ru on alumina monolith catalysts is highly active, exhibiting reaction rates competitive with precious metal catalysts, and is recyclable for up to five trials as tested with no significant loss in activity from trials 2 to 5. Notably, the millimeter-sized materials are robust, and facile to handle and separate from reaction solutions.

## 2. Results and Discussion

*Synthesis and Characterization:* Prospective catalysts were prepared by coating 2–4 mm diameter spherical  $\text{Al}_2\text{O}_3$  monoliths (Figure 1A) with an ultrathin layer of Ru by ALD. Growth was achieved utilizing an A-B cycle of alternating  $\eta^4$ -2,3-dimethylbutadiene ruthenium tricarbonyl ( $\text{Ru}(\text{DMBD})(\text{CO})_3$ ) as a zero-valent ruthenium precursor and water as a co-reactant (Figure 1B). Previous work from one of our groups has shown this specific process to produce metallic Ru [39]. Using A-B cycle sets of 50 and 75, two different materials were prepared: denoted as  $\text{Ru}_{50}@\text{Al}_2\text{O}_3$  and  $\text{Ru}_{75}@\text{Al}_2\text{O}_3$ , respectively. In this instance, the as-deposited Ru materials are a combination of metallic  $\text{Ru}^0$  and  $\text{Ru}^{4+}$  oxides. Further details are provided in the Materials and Methods.

To delineate the effect of Ru deposition on pore size,  $\text{N}_2$  physisorption was performed on an uncoated “blank”  $\text{Al}_2\text{O}_3$  sphere,  $\text{Ru}_{50}@\text{Al}_2\text{O}_3$  and  $\text{Ru}_{75}@\text{Al}_2\text{O}_3$  (Figure 1C). The blank displayed a bimodal pore size distribution with the bulk of pore radii between 13.25 and 20.25 Å with pore volumes of 0.009–0.071 cc/g, respectively. After 50 ( $\text{Ru}_{50}@\text{Al}_2\text{O}_3$ ) and 75 cycles ( $\text{Ru}_{75}@\text{Al}_2\text{O}_3$ ), the pore volume centered around pore radii of 20.25 Å decreased to 0.031 and 0.029 cc/g, respectively, and pore volumes centered around pore radii of 13.25 Å increased to 0.013 and 0.014 cc/g, respectively. This result is attributed to the Ru deposition and conformal coverage of the porous network ultimately reducing the total volume and increasing the number of smaller pores. The increase in pore radius after 75 cycles compared to the blank may be due to changes in the internal structure during ALD. Overall, the total pore volume decreased as the Ru deposition constricted the pores after ALD; this is consistent with prior literature [39,40].

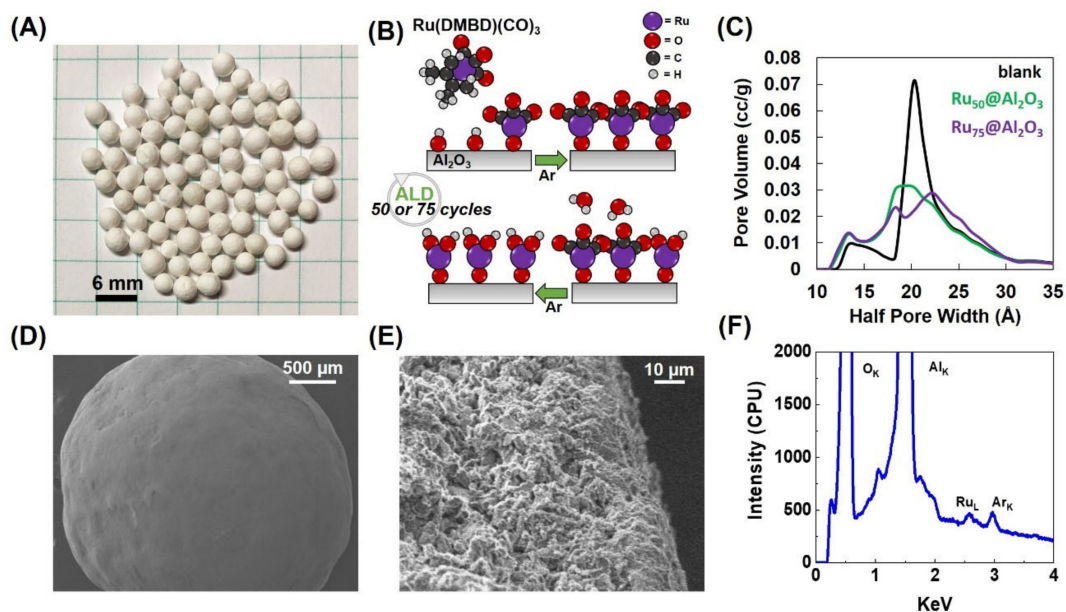


**Figure 1.** Blank  $\text{Al}_2\text{O}_3$  spheres (A); schematic representation for atomic layer deposition (ALD) growth of Ru film (B); pore volume (C); Scanning Electron Microscopy (SEM) micrographs (D,E); Energy Dispersive X-ray analysis (EDX) of  $\text{Ru}_{75}@Al_2O_3$  (F).

The surface morphology of  $\text{Ru}_{75}@Al_2O_3$  was imaged by Scanning Electron Microscopy (SEM) (Figure 1D,E). The material exhibits a complex microstructure with numerous fissures and pores commensurate with the findings of the  $\text{N}_2$  sorption analysis. Energy Dispersive X-ray analysis (EDX) of the surface was used *qualitatively*. Nonetheless, EDX confirmed the deposition of Ru (Figure 1F) as well as oxygen, aluminum, and argon (Ar). The presence of Ar can be attributed to the Ar gas used in the purge steps of the ALD super cycles. Mass percent of Ru for both materials was determined via inductively coupled plasma mass spectrometry (ICP-MS)— $1.70 \times 10^{-3} \pm 3.63 \times 10^{-4}\%$  by mass for  $\text{Ru}_{50}@Al_2O_3$  and  $1.98 \times 10^{-3} \pm 1.04 \times 10^{-4}\%$  by mass for  $\text{Ru}_{75}@Al_2O_3$ . The increase in Ru loading is commensurate with the 50% increase in number of ALD cycles. Our initial attempt to characterize the nature of Ru by XPS on  $\text{Ru}_{50}@Al_2O_3$  did not result in a significant Ru signal. We can attribute this to the highly porous structure of the  $\text{Al}_2O_3$  sphere and the presence of high C on this surface. It is to be noted that the Ru-3d signal (280.1 with a spin-orbit splitting of 4.17 eV) strongly overlapped with carbon-1s (284.5 eV), making the analysis necessarily difficult in the first place. These results suggest that a simpler analogue to monitor the chemical state of Ru on  $\text{Al}_2O_3$  needs to be formulated. Therefore, we have taken a planar substrate consisting of a Si wafer with 10 nm of  $\text{Al}_2O_3$  deposited using ALD followed by 5 nm of ALD Ru. This system reasonably represents the chemical nature of the Ru that is present on the  $\text{Al}_2O_3$  spheres without the surface topological complexity and porosity that the  $\text{Al}_2O_3$  spheres present. Therein, the Ru is a mixture of metal ( $\text{Ru}^0$ ) and  $\text{Ru}^{4+}$  at 43.22 and 56.78 atomic %, respectively (Figure S1, Table S1).

**Catalytic Testing:** The catalytic activity towards the reduction of 4NP of both materials was tested in the presence of excess  $\text{NaBH}_4$ . To validate both the ease of handling and recyclability of the catalysts, five consecutive recycle trials were performed. This was repeated a second time and the results were averaged. Reactions were conducted in a 1 cm quartz cell and monitored directly by UV-Vis spectroscopy for the decrease in absorbance for 4NP\* at  $\lambda_{\text{max}} = 400$ ; 4NP is deprotonated to form 4-nitrophenolate (4NP\*) in the presence of excess  $\text{NaBH}_4$ . This decrease in absorbance was accompanied by an increase at  $\lambda_{\text{max}} = 300$  nm, pertaining to the formation of 4-aminophenolate (4AMP\*) (Scheme 1). As noted in the introduction (*vide supra*), the reaction is typically interpreted

according to the Langmuir–Hinshelwood model, and due to the large excess of H-source ( $\text{NaBH}_4$ ), the kinetics are treated as a pseudo-first-order process. Thus it was surprising that the initial catalytic trial for both  $\text{Ru}_{50}@Al_2O_3$  and  $\text{Ru}_{75}@Al_2O_3$  could be fitted with superior confidence to a zero-order process (Figure 2A,B). However, subsequent recycle trials (2–5) for both materials yielded kinetics which fit a first-order process. We attributed this to leaching of very reactive Ru-based species upon introduction to a high pH ( $\sim 10.4$ )  $\text{NaBH}_4$ -rich environment. This likely creates an environment with multiple active catalysts, prohibiting the clear determination of a reaction order. Subsequent trials show remarkably steady performances, commensurate with a robust, highly recyclable catalyst.



Scheme 1. Reduction of 4-nitrophenol (4NP) in water with large excess  $\text{NaBH}_4$ .

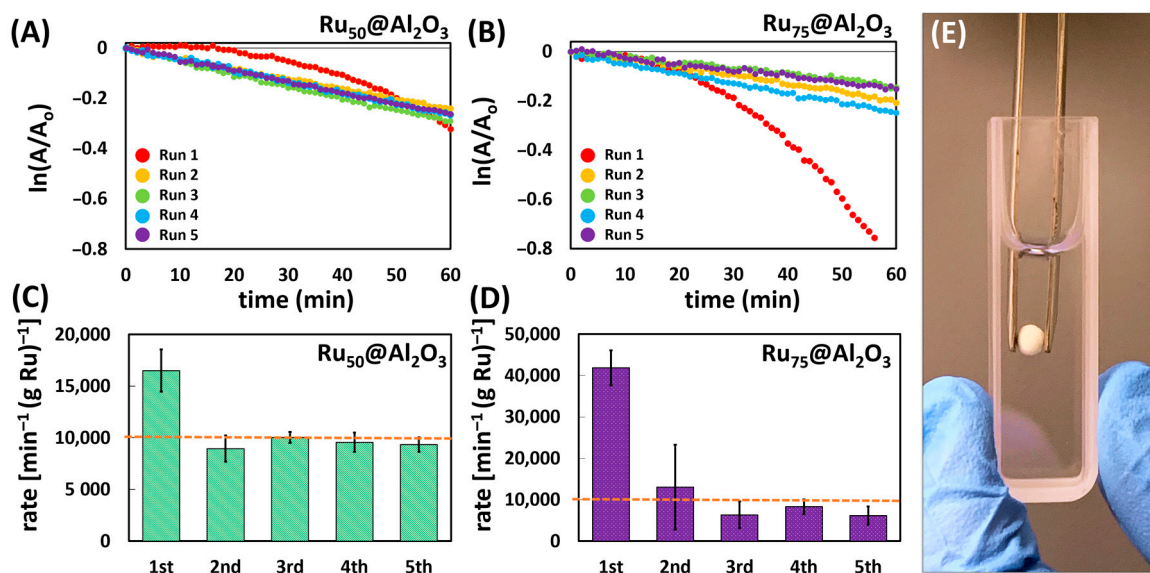


Figure 2. One 5-trial sequence of pseudo-first-order kinetics plotted for the reduction of 4NP using  $\text{Ru}_{50}@Al_2O_3$  (A) and  $\text{Ru}_{75}@Al_2O_3$  (B). Kinetic rates normalized to the mass of Ru over five trials for the  $\text{Ru}_{50}@Al_2O_3$  (C) and  $\text{Ru}_{75}@Al_2O_3$  (D); dashed line shown to facilitate rate comparison. (E) Photograph highlighting ease of handling.

Interestingly, while the mass-normalized (to Ru) observed rates ( $K$ ) for  $\text{Ru}_{50}@Al_2O_3$  and  $\text{Ru}_{75}@Al_2O_3$  differed dramatically in the initial run ( $\text{Ru}_{50}@Al_2O_3$   $K = 16,500 \pm 2042 \text{ min}^{-1}\text{g}_{\text{Ru}}^{-1}$ ;  $\text{Ru}_{75}@Al_2O_3$   $K = 41,857 \pm 4235 \text{ min}^{-1}\text{g}_{\text{Ru}}^{-1}$ ), they rapidly normalize to ca.  $K = 10,000 \text{ min}^{-1}\text{g}_{\text{Ru}}^{-1}$  for both catalysts in recycle trials 2–5 (Figure 2A–D). We postulate this similarity in trials 2–5 regardless of initial Ru loading is likely due to the presence of loosely bound surface species which arise after an initial coating threshold is reached after  $X$  number of ALD cycles ( $X < 50$ ). Thus, Ru deposited beyond this threshold is amenable to leaching, likely as highly reactive nanoparticles. Accordingly, the higher loading  $\text{Ru}_{75}@Al_2O_3$  yielded a higher observed rate in the first run due to more catalytically active material being released into the solution.

To corroborate the proposed leaching, the reaction solution post reduction of 4NP using  $\text{Ru}_{50}@Al_2O_3$  (trial 1) was measured by ICP-MS. The initial solution leached  $1.83 \times 10^{-3} \pm 2.27 \times 10^{-4} \mu\text{g Ru}/\text{mg catalyst}$ . Repeating the ICP-MS measurement under similar conditions upon completion of trial 2 indicated that  $3.80 \times 10^{-4} \pm 1.77 \times 10^{-5} \mu\text{g Ru}/\text{mg}$

leached—a nearly five-fold decrease. The mass percent of Ru on Ru<sub>50</sub>@Al<sub>2</sub>O<sub>3</sub> after all five consecutive trials was determined to be  $1.63 \times 10^{-3} \pm 1.32 \times 10^{-4}\%$  Ru by mass compared to  $1.70 \times 10^{-3} \pm 3.63 \times 10^{-4}\%$  for Ru<sub>50</sub>@Al<sub>2</sub>O<sub>3</sub> prior to catalysis. Thus, for Ru<sub>50</sub>@Al<sub>2</sub>O<sub>3</sub>, the Ru coating is remarkably stable and overall the catalyst is robust, particularly from trials 2–5. However, the small amount of Ru that does leach during the initial trial clearly forms highly reactive nanoparticles which accounts for the intractable observed kinetics; once these particles are removed from the system, the catalyst behavior is remarkably consistent.

Notably, the mass-normalized observed rate of ca.  $K = 10,000 \text{ min}^{-1} \text{g}_{\text{Ru}}^{-1}$  attained in trials 2–5 for both catalysts is very competitive. To allow comparison to other, highly reactive systems from the literature, we further normalized to reaction volume, yielding an “activity parameter”  $\kappa$  ( $\text{s}^{-1} \text{g}^{-1} \text{L}$ ) [41–43]. Therein, our catalysts had a  $\kappa$  value of ca.  $0.5 \text{ s}^{-1} \text{g}^{-1} \text{L}$ . This is competitive with a number of recent literature reports for highly active precious metal nanoparticles: Au@Fe<sub>3</sub>O<sub>4</sub> ( $0.061 \text{ s}^{-1} \text{g}^{-1} \text{L}$ ) [44]; Pd@Fe<sub>3</sub>O<sub>4</sub>/dextran ( $3.65 \text{ s}^{-1} \text{g}^{-1} \text{L}$ ) [42]; Pd@Fe<sub>3</sub>O<sub>4</sub>/SiO<sub>2</sub> ( $0.402 \text{ s}^{-1} \text{g}^{-1} \text{L}$ ) [45]; Pd@C<sub>amorphous</sub> ( $1.67 \text{ s}^{-1} \text{g}^{-1} \text{L}$ ) [43]. To confirm that no reactivity could be attributed to the Al<sub>2</sub>O<sub>3</sub> support, a blank trial was conducted with an uncoated sphere and no conversion was observed (Figure S4). To further validate the broader substrate scope and potential for our catalyst system, as a proof of concept, we tested the single run activity of Ru<sub>75</sub>@Al<sub>2</sub>O<sub>3</sub> towards the reduction of several amino-nitrophenols and azo dyes (methyl red and methyl orange). The catalyst performed well, and similar trends with respect to superior fitting to zero-order vs. first-order kinetics were observed. Further details are provided in the Supporting Information (Figures S5–S8).

For the initial run with both catalysts, there was a noteworthy induction period (10–25 min) before the reaction proceeds. This induction period is common among previously reported 4NP catalytic reductions and has been attributed to a number of effects including catalyst surface restructuring [11,46–50], or more recently due to the effects of dissolved oxygen [51–53] and the influence of surface ligands [52]. In our case, dissolved O<sub>2</sub> was clearly present both in the solution and likely within the monolith pore structure and was likely a significant contributor to the initial induction period, thus negating significant contribution from surface ligands (note, no efforts were made to exclude dissolved O<sub>2</sub>). The decomposition/leaching of the ALD-adlayer, which includes both ligands and loosely bound Ru species, also cannot be ignored as a contributor to the induction period as ICP-MS points to an initial Ru mass loss after trial 1 which quickly stabilizes over subsequent trials. This initial leaching is also commensurate with the very high initial  $k_{app}$  observed due to what we postulate to be release of very small and highly active Ru-based nanoparticles. This loss of material invariably causes some surface restructuring. Furthermore, the subsequent stability and lack of induction period in trials 2–5 are attributed to both the removal of this adlayer and weakly bound surface Ru, as well as the effect of a BH<sub>4</sub><sup>−</sup> “treatment” in trial 1, which served to remove adsorbed O<sub>2</sub> from the monolith; dissolved O<sub>2</sub> in subsequent trials was not excluded from the reaction solution so its effects were not excluded, but are comparatively minimal with respect to the induction period. Overall, beyond trial 1, the catalysts remain very reactive and consistent. When compounded with the ease of handling/manipulation as pictured in Figure 2E, the ALD-Ru@Al<sub>2</sub>O<sub>3</sub> monolith platform is a facile, robust, and effective catalyst system.

As reactions were conducted in a UV-Vis cuvette with no external agitation, the obtained rates were mass-transport limited; concomitant evolution of H<sub>2</sub> from NaBH<sub>4</sub> hydrolysis does, however, facilitate enhanced mixing compared to a completely non-agitated solution. To validate mass-transport effects, we conducted a separate set of 4NP reduction experiments with a UV-Vis dip-probe in a stirred solution. While reaction volume and reagent concentrations were scaled six-fold, a single sphere of Ru<sub>50</sub>@Al<sub>2</sub>O<sub>3</sub> was used to minimize H<sub>2</sub> evolution which causes gas bubble build-up on the probe, thus hampering accurate measurement. To negate the effects of Ru-leaching (vide supra), the sphere was pretreated with NaBH<sub>4</sub>. Subsequent measurements fit well to pseudo-first-order kinetics (Figure S9). Reactions conducted at 0, 250, 500, and 1000 rpm showed a clear

increase in observed rate as a function of stirring rate (Figure 3). At 1000 rpm, Ru<sub>50</sub>@Al<sub>2</sub>O<sub>3</sub> exhibited a  $\kappa$  value of ca.  $7.2 \text{ s}^{-1}\text{g}^{-1}\text{L}$ . Further details are provided in the Supporting Information.

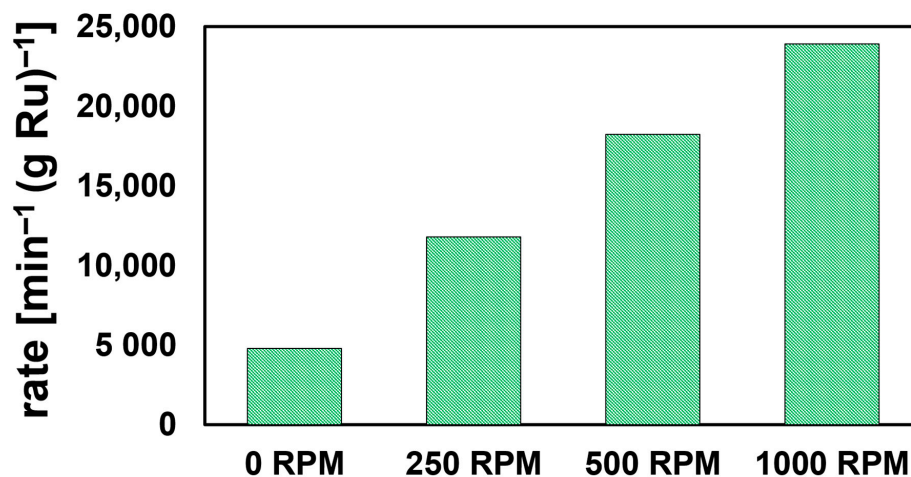


Figure 3. Ru mass-normalized pseudo-first-order kinetics plotted for the reduction of 4NP using NaBH<sub>4</sub>-pretreated Ru<sub>50</sub>@Al<sub>2</sub>O<sub>3</sub> at different stir rates (*rpm* = revolutions per minute).

### 3. Materials and Methods

**ALD:** Atomic layer deposition of ruthenium was performed using a home-built system coupled with a downstream quadrupole mass spectrometer (QMS), as described in our previous work [39,54–56]. Briefly, we used a load-locked, hot-wall, viscous flow reactor, 24 in. long with a 2.5 in. internal diameter, with an internal base pressure of  $6.1 \times 10^{-3}$  Torr as monitored by a Piezo/Pirani Dual Transducer (Model No TRN-910) from A&N Corporation. Purge gas control was obtained using a mass flow controller (Parker, 601 Series) and all the valves were pneumatically controlled ALD Valves (Swagelok). Ru(DMBD)(CO)<sub>3</sub> (EMD Performance Materials) and DIW were used for the metal film deposition onto alumina supports (from Sorbtech). The Ru(DMBD)(CO)<sub>3</sub> and DIW reactants were kept at  $25 \pm 1$  °C. The ALD furnace temperature was held at 185 °C and the inlet gas lines were held at 80 °C. Ru(DMBD)(CO)<sub>3</sub> was stored in a stainless steel bubbler and was carried into the reaction chamber by 99.999% pure Ar gas at rate of 25 standard cubic centimeters per minute (sccm) for 5 s. Each Ru(DMBD)(CO)<sub>3</sub> pulse was followed by a purge step of 75 sccm Ar for 25 s. A subsequent vacuum step returned the chamber pressure to baseline before the following reactant DIW was directly introduced from a single outlet ampoule for 2s. The purge step followed with 75 sccm Ar for 25 s then a vacuum step to finish the super cycle. The reaction mechanism is described by Gao et al. [39], where a growth rate on planar silicon substrate of 1 Å/cycle is reported.

For deposition on Al<sub>2</sub>O<sub>3</sub> spheres, a batch of 20× spheres were loaded inside a “steel barrel” mini-reactor. The mini-reactor had an inlet and exhaust port to allow the flow of gases inside the holder, exposing the Al<sub>2</sub>O<sub>3</sub> spheres to the ALD chemistry. Details of this procedure will be provided in a subsequent publication. The mini-reactor was then inserted inside the ALD furnace. The reactor was rotated on its cylindrical axis by magnetically coupling it to an external servo motor (from Transfer Engineering and Manufacturing Inc.<sup>®</sup>, Fremont, CA, USA). The rotations per minute (rpm) were fixed at 8 rpm. Each cycle was repeated 50 and 75 times to create varying thicknesses of Ru deposition on Al<sub>2</sub>O<sub>3</sub> spheres targeting thicknesses of 50 and 75 Å, respectively.

**Characterization:** A JEOL JSM-6480 SEM was used to record images at 5.0 kV of a blank sphere. Additionally, EDX analysis was completed on Ru<sub>75</sub>@Al<sub>2</sub>O<sub>3</sub> with a beam energy of 15.00 kV at a 15 mm working distance to verify Ru deposition. Nitrogen sorption isotherms were measured at 77 K with a Quantachrome Autosorb iQ. Before measurements, the samples were degassed in a vacuum at 400 °C for 1 h. The Brunauer–Emmett–Teller

method was utilized to calculate the specific surface areas using adsorption data in a relative pressure range from 0.05 to 0.35. The pore volumes and pore size distributions were calculated using the density functional theory model. Ru mass percent was determined through ICP-MS using an iCAP RQ ThermoScientific mass spectrometer. Ru-101 was used as the isotope of analysis, and kinetic energy discrimination (KED mode) was utilized to minimize interferences. To prepare the analysis solution, each sphere was crushed and dissolved in nearly boiling 10 M plasma grade sodium hydroxide (Thermo) and diluted to ~2% plasma grade nitric acid (Thermo). The content was compared to a calibration curve using standard Ru (American Standards, plasma grade, 1000 mg L<sup>-1</sup>). Three analysis solutions for each catalyst were prepared and three readings of each solution were performed and averaged. To test for Ru-metal leaching, a similar protocol was performed on the solution remaining post 4NP reduction and physical removal of Ru<sub>50</sub>@Al<sub>2</sub>O<sub>3</sub>.

**Catalytic Investigations:** UV-Vis measurements were carried out using an Agilent Cary 60 spectrophotometer under ambient conditions. Solutions were prepared in 1 cm quartz cuvettes and the reaction solution was scanned at timed intervals of 1 min. The 4NP solutions were prepared by dissolving 0.39 μmol of 4NP and 0.2 mmol of NaBH<sub>4</sub> in 3 mL of DIW. Five consecutive runs were completed with a DIW rinse between each run. Reaction rates were monitored by the decreasing absorbance at λ<sub>max</sub> = 400 nm (4NP\*). Dip-probe reactions to delineate effects of stirring rate were carried out using an Agilent Cary 60 spectrophotometer with optical dip-probe under ambient conditions and monitored similarly as mentioned above. The 4NP solutions were prepared by dissolving 2.34 μmol of 4NP and 1.2 mmol of NaBH<sub>4</sub> in 18 mL of DIW.

#### 4. Conclusions

The use of ALD facilitates the controllable ultralow loading of the semiprecious metal Ru on commercially available Al<sub>2</sub>O<sub>3</sub> monoliths with no additional pre- or post-treatments. The resulting catalysts, Ru<sub>50</sub>@Al<sub>2</sub>O<sub>3</sub> and Ru<sub>75</sub>@Al<sub>2</sub>O<sub>3</sub>, provide a stable and highly recyclable platform for the reduction of environmentally relevant, and the reduction catalysis benchmark, substrate 4NP. The normalized observed rates are competitive with typical precious metal-based nanoparticle species (e.g., Pd and Au). Critically, the millimeter-sized Al<sub>2</sub>O<sub>3</sub> platform allows for truly facile handling and recyclability, which when coupled with the robust nature of the material is promising for future applications in both pollutant remediation and organic transformations.

**Supplementary Materials:** The following are available online at <https://www.mdpi.com/2073-4344/11/2/165/s1>, Figure S1: XPS analysis of model ALD Ru on Al<sub>2</sub>O<sub>3</sub> film, Table S1: atomic % Ru by XPS, Figure S2: UV-Vis spectra and kinetics for the Ru<sub>50</sub>@Al<sub>2</sub>O<sub>3</sub> reduction of 4NP, Table S2: 1st and 0th order kinetics for the Ru<sub>50</sub>@Al<sub>2</sub>O<sub>3</sub> reduction of 4NP, Figure S3: UV-Vis spectra and kinetics for the Ru<sub>75</sub>@Al<sub>2</sub>O<sub>3</sub> reduction of 4NP, Table S3: 1st and 0th order kinetics for the Ru<sub>75</sub>@Al<sub>2</sub>O<sub>3</sub> reduction of 4NP, Figure S4: UV-Vis spectra for the blank Al<sub>2</sub>O<sub>3</sub> sphere test for reduction of 4NP, Figures S5–S8: reduction of other nitro and azo-based molecules, and Figures S9 and S10: reduction of 4NP with stirring.

**Author Contributions:** Conceptualization, T.J., P.B., C.F. and L.R.S.; methodology, T.J., P.B., L.R.S. and C.F.; synthesis, C.F. and Z.G.; catalysis, L.R.S.; ICP-MS, J.S., and V.A.A.; SEM and EDS, C.F.; BET, S.X. and F.L.; writing—original draft preparation and review and editing, L.R.S., T.J., C.F., P.B., F.L. and V.A.A.; supervision, T.J., P.B., F.L. and V.A.A. All authors have read and agreed to the published version of the manuscript.

**Funding:** This research received no external funding.

**Institutional Review Board Statement:** Not applicable.

**Informed Consent Statement:** Not applicable.

**Data Availability Statement:** Data is contained in the article and supplementary material. Any additional data are available on request from the corresponding author.

**Acknowledgments:** Authors acknowledge the NSF MRI: ECCS: 1726636 and MCF-AMPAC facility, MSE and CECS. Z.G. acknowledges support from the Preeminent Postdoctoral Program (P3) fellowship at the University of Central Florida. P.B. and C.F. acknowledge support from the National Science Foundation (NSF) under Award No. 1808625. Support from EMD Performance Materials(c) for supplying the Ru precursor molecule Ru(DMBD)(CO)<sub>3</sub> is acknowledged.

**Conflicts of Interest:** The authors declare no conflict of interest.

## References

1. Aditya, T.; Pal, A.; Pal, T. Nitroarene reduction: A trusted model reaction to test nanoparticle catalysts. *Chem. Commun.* **2015**, *51*, 9410–9431. [[CrossRef](#)]
2. Begum, R.; Rehan, R.; Farooqi, Z.H.; Butt, Z.; Ashraf, S. Physical chemistry of catalytic reduction of nitroarenes using various nanocatalytic systems: Past, present, and future. *J. Nanoparticle Res.* **2016**, *18*, 231. [[CrossRef](#)]
3. Song, J.; Huang, Z.-F.; Pan, L.; Li, K.; Zhang, X.; Wang, L.; Zou, J.-J. Review on selective hydrogenation of nitroarene by catalytic, photocatalytic and electrocatalytic reactions. *Appl. Catal. B Environ.* **2018**, *227*, 386–408. [[CrossRef](#)]
4. Herves, P.; Pérez-Lorenzo, M.; Liz-Marzán, L.M.; Dzubiel, J.; Lu, Y.; Ballauff, M. Catalysis by metallic nanoparticles in aqueous solution: Model reactions. *Chem. Soc. Rev.* **2012**, *41*, 5577–5587. [[CrossRef](#)]
5. Kadam, H.K.; Tilve, S.G. Advancement in methodologies for reduction of nitroarenes. *RSC Adv.* **2015**, *5*, 83391–83407. [[CrossRef](#)]
6. Zhao, P.; Feng, X.; Huang, D.; Yang, G.; Astruc, D. Basic concepts and recent advances in nitrophenol reduction by gold-and other transition metal nanoparticles. *Coord. Chem. Rev.* **2015**, *287*, 114–136. [[CrossRef](#)]
7. Bingwa, N.; Meijboom, R. Kinetic evaluation of dendrimer-encapsulated palladium nanoparticles in the 4-nitrophenol reduction reaction. *J. Phys. Chem. C* **2014**, *118*, 19849–19858. [[CrossRef](#)]
8. Dolatkhan, A.; Jani, P.; Wilson, L.D. Redox-responsive polymer template as an advanced multifunctional catalyst support for silver nanoparticles. *Langmuir* **2018**, *34*, 10560–10568. [[CrossRef](#)]
9. Gopalakrishnan, R.; Loganathan, B.; Dinesh, S.; Raghu, K. Strategic green synthesis, characterization and catalytic application to 4-nitrophenol reduction of palladium nanoparticles. *J. Clust. Sci.* **2017**, *28*, 2123–2131. [[CrossRef](#)]
10. Islam, M.T.; Saenz-Arana, R.; Wang, H.; Bernal, R.; Noveron, J.C. Green synthesis of gold, silver, platinum, and palladium nanoparticles reduced and stabilized by sodium rhodizonate and their catalytic reduction of 4-nitrophenol and methyl orange. *New J. Chem.* **2018**, *42*, 6472–6478. [[CrossRef](#)]
11. Mei, Y.; Sharma, G.; Lu, Y.; Ballauff, M.; Drechsler, M.; Irrgang, T.; Kempe, R. High catalytic activity of platinum nanoparticles immobilized on spherical polyelectrolyte brushes. *Langmuir* **2005**, *21*, 12229–12234. [[CrossRef](#)] [[PubMed](#)]
12. Pandey, S.; Mishra, S.B. Catalytic reduction of p-nitrophenol by using platinum nanoparticles stabilised by guar gum. *Carbohydr. Polym.* **2014**, *113*, 525–531. [[CrossRef](#)] [[PubMed](#)]
13. Zhang, K.; Liu, Y.; Deng, J.; Xie, S.; Lin, H.; Zhao, X.; Yang, J.; Han, Z.; Dai, H. Fe<sub>2</sub>O<sub>3</sub>/3DOM BiVO<sub>4</sub>: High-performance photocatalysts for the visible light-driven degradation of 4-nitrophenol. *Appl. Catal. B Environ.* **2017**, *202*, 569–579. [[CrossRef](#)]
14. Shultz, L.R.; McCullough, B.; Newsome, W.J.; Ali, H.; Shaw, T.E.; Davis, K.O.; Uribe-Romo, F.J.; Baudelet, M.; Jurca, T. A Combined Mechanochemical and Calcination Route to Mixed Cobalt Oxides for the Selective Catalytic Reduction of Nitrophenols. *Molecules* **2020**, *25*, 89. [[CrossRef](#)]
15. Mogudi, B.M.; Ncube, P.; Bingwa, N.; Mawila, N.; Mathebula, S.; Meijboom, R. Promotion effects of alkali-and alkaline earth metals on catalytic activity of mesoporous Co<sub>3</sub>O<sub>4</sub> for 4-nitrophenol reduction. *Appl. Catal. B Environ.* **2017**, *218*, 240–248. [[CrossRef](#)]
16. Chinnappan, A.; Eshkalak, S.K.; Baskar, C.; Khatibzadeh, M.; Kowsari, E.; Ramakrishna, S. Flower-like 3-dimensional hierarchical Co<sub>3</sub>O<sub>4</sub>/NiO microspheres for 4-nitrophenol reduction reaction. *Nanoscale Adv.* **2019**, *1*, 305–313. [[CrossRef](#)]
17. Aditya, T.; Jana, J.; Singh, N.K.; Pal, A.; Pal, T. Remarkable Facet Selective Reduction of 4-Nitrophenol by Morphologically Tailored (111) Faceted Cu<sub>2</sub>O Nanocatalyst. *ACS Omega* **2017**, *2*, 1968–1984. [[CrossRef](#)]
18. Wang, Z.; Su, R.; Wang, D.; Shi, J.; Wang, J.-X.; Pu, Y.; Chen, J.-F. Sulfurized graphene as efficient metal-free catalysts for reduction of 4-nitrophenol to 4-aminophenol. *Ind. Eng. Chem. Res.* **2017**, *56*, 13610–13617. [[CrossRef](#)]
19. Nasrollahzadeh, M.; Nezafat, Z.; Gorab, M.G.; Sajjadi, M. Recent progresses in graphene-based (photo)catalysts for reduction of nitro compounds. *Mol. Catal.* **2020**, *484*, 110758. [[CrossRef](#)]
20. Kong, X.-K.; Sun, Z.-Y.; Chen, M.; Chen, Q.-W. Metal-free catalytic reduction of 4-nitrophenol to 4-aminophenol by N-doped graphene. *Energy Environ. Sci.* **2013**, *6*, 3260–3266. [[CrossRef](#)]
21. Gao, L.; Li, R.; Sui, X.; Li, R.; Chen, C.; Chen, Q. Conversion of chicken feather waste to N-doped carbon nanotubes for the catalytic reduction of 4-nitrophenol. *Environ. Sci. Technol.* **2014**, *48*, 10191–10197. [[CrossRef](#)] [[PubMed](#)]
22. Zhang, W.; Xiao, B.; Fang, T. Chemical transformation of silver nanoparticles in aquatic environments: Mechanism, morphology and toxicity. *Chemosphere* **2018**, *191*, 324–334. [[CrossRef](#)] [[PubMed](#)]
23. Smita, S.; Gupta, S.K.; Bartonova, A.; Dusinska, M.; Gutleb, A.C.; Rahman, Q. Nanoparticles in the environment: Assessment using the causal diagram approach. *Environ. Health* **2012**, *11*, S13. [[CrossRef](#)] [[PubMed](#)]
24. Roy, R.; Kumar, S.; Tripathi, A.; Das, M.; Dwivedi, P.D. Interactive threats of nanoparticles to the biological system. *Immunol. Lett.* **2014**, *158*, 79–87. [[CrossRef](#)] [[PubMed](#)]

25. Neal, A.L. What can be inferred from bacterium–nanoparticle interactions about the potential consequences of environmental exposure to nanoparticles? *Ecotoxicology* **2008**, *17*, 362. [[CrossRef](#)]
26. Liu, W.-T. Nanoparticles and their biological and environmental applications. *J. Biosci. Bioeng.* **2006**, *102*, 1–7. [[CrossRef](#)]
27. Ghosh, M.; Ghosh, I.; Godderis, L.; Hoet, P.; Mukherjee, A. Genotoxicity of engineered nanoparticles in higher plants. *Mutat. Res./Genet. Toxicol. Environ. Mutagen.* **2019**, *842*, 132–145. [[CrossRef](#)]
28. Biswas, P.; Wu, C.-Y. Nanoparticles and the Environment. *J. Air Waste Manag. Assoc.* **2005**, *55*, 708–746. [[CrossRef](#)]
29. Zhang, J.; Chen, C.; Yan, W.; Duan, F.; Zhang, B.; Gao, Z.; Qin, Y. Ni nanoparticles supported on CNTs with excellent activity produced by atomic layer deposition for hydrogen generation from the hydrolysis of ammonia borane. *Catal. Sci. Technol.* **2016**, *6*, 2112–2119. [[CrossRef](#)]
30. Zhang, J.; Chen, C.; Chen, S.; Hu, Q.; Gao, Z.; Li, Y.; Qin, Y. Highly dispersed Pt nanoparticles supported on carbon nanotubes produced by atomic layer deposition for hydrogen generation from hydrolysis of ammonia borane. *Catal. Sci. Technol.* **2017**, *7*, 322–329. [[CrossRef](#)]
31. Nandi, D.K.; Manna, J.; Dhara, A.; Sharma, P.; Sarkar, S.K. Atomic layer deposited cobalt oxide: An efficient catalyst for NaBH<sub>4</sub> hydrolysis. *J. Vac. Sci. Technol. A* **2016**, *34*, 01A115. [[CrossRef](#)]
32. Jiang, C.; Shang, Z.; Liang, X. Chemoselective Transfer Hydrogenation of Nitroarenes Catalyzed by Highly Dispersed, Supported Nickel Nanoparticles. *ACS Catal.* **2015**, *5*, 4814–4818. [[CrossRef](#)]
33. Shvo, Y.; Czarkie, D. Catalytic reduction of nitroaromatics with carbon monoxide and water using tricarbonyltetraphenylcyclopentadienone ruthenium(0). *J. Organomet. Chem.* **1989**, *368*, 357–365. [[CrossRef](#)]
34. Liu, Y.; Chen, W.; Feng, C.; Deng, G. Ruthenium-Catalyzed One-Pot Aromatic Secondary Amine Formation from Nitroarenes and Alcohols. *Chem. Asian J.* **2011**, *6*, 1142–1146. [[CrossRef](#)] [[PubMed](#)]
35. Rambabu, D.; Pradeep, C.P.; Dhir, A. New self-assembled material based on Ru nanoparticles and 4-sulfocalix[4]arene as an efficient and recyclable catalyst for reduction of brilliant yellow azo dye in water: A new model catalytic reaction. *J. Nanopart. Res.* **2016**, *18*, 381. [[CrossRef](#)]
36. Kim, J.H.; Park, J.H.; Chung, Y.K.; Park, K.H. Ruthenium Nanoparticle-Catalyzed, Controlled and Chemoselective Hydrogenation of Nitroarenes using Ethanol as a Hydrogen Source. *Adv. Synth. Catal.* **2012**, *354*, 2412–2418. [[CrossRef](#)]
37. Hemraj-Benny, T.; Tobar, N.; Carrero, N.; Sumner, R.; Pimentel, L.; Emeran, G. Microwave-assisted synthesis of single-walled carbon nanotube-supported ruthenium nanoparticles for the catalytic degradation of Congo red dye. *Mater. Chem. Phys.* **2018**, *216*, 72–81. [[CrossRef](#)]
38. Carrillo, A.I.; Stampelcoskie, K.G.; Marin, M.L.; Scaiano, J.C. ‘From the mole to the molecule’: Ruthenium catalyzed nitroarene reduction studied with ‘bench’, high-throughput and single molecule fluorescence techniques. *Catal. Sci. Technol.* **2014**, *4*, 1989–1996. [[CrossRef](#)]
39. Gao, Z.; Le, D.; Khaniya, A.; Dezelah, C.L.; Woodruff, J.; Kanjolia, R.K.; Kaden, W.E.; Rahman, T.S.; Banerjee, P. Self-Catalyzed, Low-Temperature Atomic Layer Deposition of Ruthenium Metal Using Zero-Valent Ru(DMBD)(CO)<sub>3</sub> and Water. *Chem. Mater.* **2019**, *31*, 1304–1317. [[CrossRef](#)]
40. Detavernier, C.; Dendooven, J.; Sree, S.P.; Ludwig, K.F.; Martens, J.A. Tailoring nanoporous materials by atomic layer deposition. *Chem. Soc. Rev.* **2011**, *40*, 5242–5253. [[CrossRef](#)]
41. Kästner, C.; Thünemann, A.F. Catalytic Reduction of 4-Nitrophenol Using Silver Nanoparticles with Adjustable Activity. *Langmuir* **2016**, *32*, 7383–7391. [[CrossRef](#)] [[PubMed](#)]
42. Lara, L.R.S.; Zottis, A.D.; Elias, W.C.; Faggion, D.; Maduro de Campos, C.E.; Acuña, J.J.S.; Domingos, J.B. The catalytic evaluation of in situ grown Pd nanoparticles on the surface of Fe<sub>3</sub>O<sub>4</sub>@dextran particles in the p-nitrophenol reduction reaction. *RSC Adv.* **2015**, *5*, 8289–8296. [[CrossRef](#)]
43. Shultz, L.R.; Hu, L.; Preradovic, K.; Beazley, M.J.; Feng, X.; Jurca, T. Cover Feature: A Broader-scope Analysis of the Catalytic Reduction of Nitrophenols and Azo Dyes with Noble Metal Nanoparticles. *ChemCatChem* **2019**, *11*, 2560. [[CrossRef](#)]
44. Lin, F.-H.; Doong, R.-A. Bifunctional Au–Fe<sub>3</sub>O<sub>4</sub> Heterostructures for Magnetically Recyclable Catalysis of Nitrophenol Reduction. *J. Phys. Chem. C* **2011**, *115*, 6591–6598. [[CrossRef](#)]
45. An, M.; Cui, J.; Wang, L. Magnetic Recyclable Nanocomposite Catalysts with Good Dispersibility and High Catalytic Activity. *J. Phys. Chem. C* **2014**, *118*, 3062–3068. [[CrossRef](#)]
46. Zhou, X.; Xu, W.; Liu, G.; Panda, D.; Chen, P. Size-Dependent Catalytic Activity and Dynamics of Gold Nanoparticles at the Single-Molecule Level. *J. Am. Chem. Soc.* **2010**, *132*, 138–146. [[CrossRef](#)]
47. Xu, W.; Kong, J.S.; Yeh, Y.-T.E.; Chen, P. Single-molecule nanocatalysis reveals heterogeneous reaction pathways and catalytic dynamics. *Nat. Mater.* **2008**, *7*, 992–996. [[CrossRef](#)]
48. Wunder, S.; Lu, Y.; Albrecht, M.; Ballauff, M. Catalytic activity of faceted gold nanoparticles studied by a model reaction: Evidence for substrate-induced surface restructuring. *ACS Catal.* **2011**, *1*, 908–916. [[CrossRef](#)]
49. Kalekar, A.M.; Sharma, K.K.K.; Lehoux, A.; Audonnet, F.; Remita, H.; Saha, A.; Sharma, G.K. Investigation into the Catalytic Activity of Porous Platinum Nanostructures. *Langmuir* **2013**, *29*, 11431–11439. [[CrossRef](#)]
50. Ansar, S.M.; Kitchens, C.L. Impact of Gold Nanoparticle Stabilizing Ligands on the Colloidal Catalytic Reduction of 4-Nitrophenol. *ACS Catal.* **2016**, *6*, 5553–5556. [[CrossRef](#)]
51. Menumerov, E.; Hughes, R.A.; Neretina, S. Catalytic Reduction of 4-Nitrophenol: A Quantitative Assessment of the Role of Dissolved Oxygen in Determining the Induction Time. *Nano Lett.* **2016**, *16*, 7791–7797. [[CrossRef](#)] [[PubMed](#)]

52. Neal, R.D.; Hughes, R.A.; Sapkota, P.; Ptasinska, S.; Neretina, S. Effect of Nanoparticle Ligands on 4-Nitrophenol Reduction: Reaction Rate, Induction Time, and Ligand Desorption. *ACS Catal.* **2020**, *10*, 10040–10050. [[CrossRef](#)]
53. Pradhan, N.; Pal, A.; Pal, T. Silver nanoparticle catalyzed reduction of aromatic nitro compounds. *Colloids Surf. A Physicochem. Eng. Asp.* **2002**, *196*, 247–257. [[CrossRef](#)]
54. Shi, L.; Gao, Z.; Liu, Z.; Myung, Y.; Banerjee, P. Configurational Entropy of Adlayers in Atomic Layer Deposition. *Chem. Mater.* **2017**, *29*, 5458–5462. [[CrossRef](#)]
55. Gao, Z.; Wu, F.; Myung, Y.; Fei, R.; Kanjolia, R.; Yang, L.; Banerjee, P. Standing and sitting adlayers in atomic layer deposition of ZnO. *J. Vac. Sci. Technol. A Vac. Surf. Film* **2016**, *34*, 01A143. [[CrossRef](#)]
56. Gao, Z.; Myung, Y.; Huang, X.; Kanjolia, R.; Park, J.; Mishra, R.; Banerjee, P. Doping mechanism in transparent, conducting tantalum doped ZnO films deposited using atomic layer deposition. *Adv. Mater. Interfaces* **2016**, *3*, 1600496. [[CrossRef](#)]